Pol. J. Environ. Stud. Vol. XX, No. X (XXXX), 1-17
DOI: 10.15244/pjoes/231508 ONLINE PUBLICATION DATE: 2026-11-06

Original Research

Synthesis of a Polyaniline-Modified Magnetic Zn/Fe Bimetallic Sludge Biochar for Aqueous Cr(VI) Adsorption

Xiaohan Duan[1, 2], Junkai Zheng[3], Hui Li[1], Nan Xuan[1], Muyao Chen[4], Jingxi Tie[2]*

[1]Henan Vocational College of Water Conservancy and Environment, Zhengzhou 450008, China
[2]School of Ecology and Environment, North China University of Water Resources and Electric Power, Zhengzhou 450046, China
[3]Hohai University, Nanjing 210024, China
[4]Beijing Forestry University, Beijing 100083, China

Received: 17 May 2026
Accepted: 21 August 2026

Abstract

Heavy metals are recognized as a growing environmental concern due to their toxicity and long-term stability. In this study, a magnetic composite biochar material (PDFMB) was synthesized using iron-based sludge and Chinese medicine residue, with zinc chloride and polyaniline serving as modifiers, to adsorb and reduce Cr(VI) in water. The optimal preparation conditions were determined through preliminary experiments, and the adsorption performance was evaluated through material characterization and Cr(VI) adsorption tests. The removal of Cr(VI) by PDFMB was highly pH-dependent, with an optimal pH of 2, indicating that acidic conditions favored adsorption. The maximum adsorption capacity for Cr(VI) at 308 K and pH 5 was 111.11 mg/g. The adsorption kinetics followed a pseudo-second-order model, while the Langmuir isotherm provided a good fit to the adsorption isotherm data. Thermodynamic analysis revealed that the removal process was spontaneous and endothermic. The anions Cl^-, SO_4^{2-}, and PO_4^{3-} inhibited the removal efficiency of Cr(VI), with inhibition strength following the order $Cl^-<SO_4^{2-}<PO_4^{3-}$. The key mechanisms involved in Cr(VI) removal included physical and chemical adsorption, chelation, and the reduction of Cr(VI) to Cr(III). The PDFMB composite exhibited high stability and reusability, achieving an 85.25% removal efficiency after six cycles. Owing to its high efficiency, magnetic separability, and excellent recyclability, PDFMB represents a highly promising candidate for addressing Cr(VI) pollution.

Keywords: Chinese medicine residue, iron-based waterworks sludge, polyaniline, Cr(VI), adsorption

*e-mail:15202843@qq.com
0000-0003-4614-4600

© 2026 This article is licensed under a Creative Commons Attribution-NonCommercial 4.0 International (CC BY-NC 4.0)

Introduction

Heavy metals are considered one of the most hazardous groups of pollutants among various wastewater pollutants [1] because of their potential toxicity, high mobility and non-biodegradable nature. Chromium (Cr) is a typical heavy metal used in industrial processes including paint manufacturing, electroplating, chemical manufacturing, metal plating, and tanning [2]. The US Environmental Protection Agency (US-EPA) and the World Health Organization classify Cr(VI) as the second most abundant inorganic groundwater pollutant. Hence, it is of great significance to address the Cr(VI) problem using a safe and effective approach.

Techniques including chemical precipitation, ion exchange, ultrafiltration and membrane separation for removing Cr(VI) have several limitations, such as complex procedures, high costs, and secondary chemical contamination. Considering its high efficiency and low cost, adsorption is regarded as one of the most valuable techniques for Cr(VI) removal [3]. Finding a cheap and efficient adsorbent is important for adsorption techniques. Thus, biochar generated from a series of biomass materials has been identified as a cost-effective adsorbent. Up to 70 million tons of Chinese medicine residue (CMR) is produced annually in China with the development of Chinese medicine, and is mainly disposed of as solid waste in landfills [4]. As a result, CMR is a potential resource for preparing biochar. Yuan et al. [5] prepared five types of traditional Chinese medicine residue biochars (DNS, CX, DG, DGS, HQ), which possessed favorable structural stability and removed Pb(II) with a maximum adsorption capacity of 36.42 mg/g. Nevertheless, raw medicinal residue biochar lacks magnetism to facilitate convenient solid-liquid separation after adsorption and has limited adsorption performance, so corresponding modification treatment is necessary to strengthen its practical remediation capability.

Large amounts of iron-based sludge (IS) are generated both in waterworks using iron-based coagulants and during the treatment of iron-containing groundwater [6]. Currently, the most common disposal method for this sludge is landfill, which can lead to the leaching of metal ions, contamination of soil and surface water, and harm to the environment. Zhao et al. [7] prepared Fe-modified sewage sludge biochar (Fe-HKBC), which possessed abundant iron species and oxygen-containing functional groups along with a specific surface area of 280.68 m^2/g, achieving a higher removal capacity for Cr(VI) than the original biochar. Notably, IS can be magnetized through calcination, as the iron minerals within it are converted into magnetic Fe_3O_4 particles during pyrolysis [8]. Therefore, modifying biochar with IS is a more environmentally friendly approach than traditional chemical magnetic modification methods. Zinc chloride ($ZnCl_2$) is a common activating agent that effectively increases functional groups and promotes the formation of porous structures [9]. Furthermore, the co-calcination of zinc and iron at high temperatures generates magnetic zinc ferrite ($ZnFe_2O_4$), which significantly enhances magnetism [10].

As a typical conducting polymer, polyaniline (PANI) has become a promising material owing to its extended π-conjugated skeletons, high conductivity, good stability, simple preparation, and eco-friendly and non-toxic nature [11]. Particularly, PANI contains a variety of functional groups, including amino and imine groups, which endow it with the adsorption and reduction capacities for anions, such as Cr(VI) [12]. Behera et al. [13] prepared a flower-shaped polyaniline-modified yttrium phosphate (PANI-YPO_4) composite, achieving a Cr(VI) adsorption capacity of 91.0 mg/g with outstanding structural stability. Nevertheless, the non-magnetic nature of polyaniline hinders solid–liquid separation and limits its cyclic regeneration in practical applications.

To prepare an efficient and environmentally friendly composite material, this study synthesized magnetic biochar using $ZnCl_2$ as a pore-forming agent, polyaniline as an amino grafting reagent, and iron-based sludge combined with traditional Chinese medicine residue as raw materials. The adsorption performance of the composite toward hexavalent chromium (Cr(VI)) and its physicochemical properties were investigated, and the removal mechanism of Cr(VI) was further elucidated.

Materials and Methods

Preparation of the Material

The CMR was obtained from a pharmacy in Zhengzhou, Henan, China. The IS was collected from a drinking water treatment plant in Huludao, Liaoning, China. The CMR and IS were dried at 105°C. The major elemental composition and mass fractions of iron-rich sludge (IS) were characterized by X-ray fluorescence (XRF). Table 1 shows that the mass fraction of Fe reached 78.62%, followed by C (6.54%) and Si (5.89%). These components mainly originated from iron-based flocculants and suspended organic matter in raw water, and no toxic or hazardous substances were detected in IS.

Table 1. The main element contents of IS (wt.%)

Fe	C	Si	Al	Ca	K	Mg
78.62	6.54	5.89	2.94	0.93	0.60	0.46

CMR and IS were thoroughly mixed at a mass ratio of 1:2. The mixture in the crucible was microwaved at 300 W for 10 min as a pre-treatment. Subsequently, 25 wt.% of $ZnCl_2$ was added to the CMR-IS mixture, and the material was dried at 105°C for 24 h. Calcination was carried out in a vacuum tube furnace under a nitrogen flow of 200 mL/min. The furnace was heated to 400°C at a ramp rate of 15°C/min and held at this temperature for 3 h to obtain the dual ferrite magnetic biochar (DFMB).

In the preliminary experiment, 3.5 mL of aniline was added to 100 mL of HCl solution (0.25-0.5 mol/L), and the mixture was stirred for 1 h at 300 rpm. Under the same stirring conditions, DFMB (0.5-3 g) was added and mixed for 20 min. Then, 50 mL of $(NH_4)_2S_2O_8$ solution (90 g/L) was added to the reaction system, followed by stirring for 30 min. The mixture was allowed to stand for 8 h, after which the solids were separated and dried in a vacuum oven for 12 h. The dried particles were crushed and filtered through a 60-mesh sieve to obtain polyaniline dual ferrite magnetic biochar (PDFMB) for subsequent experiments.

Static Adsorption Experiment

In the experiment, $K_2Cr_2O_7$ was dissolved in water to produce the Cr(VI) solutions. The pH was adjusted using 0.1 mol/L HCl or NaOH.

0.05 g PDFMB was added to 25 mL Cr(VI)-containing wastewater. The mixture was reacted at 120 rpm in a temperature-controlled shaker and filtered with a 0.45 μm filter membrane after adsorption. The concentration of Cr(VI) was measured using a UV–Vis spectrophotometer at 540 nm. Each experiment was performed in triplicate, and the average value was used for subsequent analysis.

Results and Discussion

Determination of the Conditions for PDFMB Preparation

The ideal PDFMB composite should possess both superior magnetic separation performance and prominent Cr(VI) adsorption capacity. All saturation magnetization and corresponding adsorption data for each preparation group are summarized in Table 2 to elucidate the trade-off between magnetic properties and adsorption capability. As shown in Fig. 1a) and c), PDFMB achieved the highest adsorption capacity when the HCl concentration was 0.5 mol/L, while it still showed great magnetism (18.1 emu/g). Fig. 1b), d indicated that increasing the dose of DFMB created a contradiction between the magnetism and the Cr(VI) removal performance of PDFMB. Fig. 1b) demonstrated that the magnetization was visibly enhanced from 6.8 emu/g to 18.1 emu/g as the dose of DFMB increased from 0.75 g to 1.5 g, while the magnetization remained basically the same as the DFMB dose increased from 1.5 g to 3 g. Fig. 1d showed that the Cr(VI) uptake decreased continuously with increasing DFMB dose. The Cr(VI) uptake decreased from 64.1 mg/g to 56.4 mg/g as the DFMB dose increased from 1.5 g to 3 g.

Table 2. SBET and pore textures of PDFMB with different condition

HCl concentration (mol/L)	Saturation magnetization (emu/g)	Cr(VI) uptake (mg/g)
0	18.7	14.1
0.25	17.9	52.4
0.5	18.1	78.5
1	23.1	70.8
1.5	19.8	70.2
2	12.9	71.5
DFMB dosage (g)	Saturation magnetization (emu/g)	Cr(VI) uptake (mg/g)
0.75	6.8	77.1
1.5	18.2	64.1
3	21.3	56.4
4.5	27.7	37.4

Excessive DFMB filler dilutes the mass fraction of PANI functional components with chelation and reduction activity within the composite matrix, thereby weakening the intrinsic adsorption efficiency per unit adsorbent mass. Considering both magnetism and Cr(VI) adsorption performance, the HCl concentration and the dose of DFMB were determined to be 0.5 mol/L and 1.5 g, respectively, for preparing PDFMB.

Sample Characterization

SEM images of DFMB, PDFMB and PDFMB after Cr(VI) adsorption are shown in Fig. 2(a-c). Fig. 2a) shows that the DFMB had spherical particles and octahedral spinel particles on its surface, which might be iron oxide (Fe_3O_4) and magnetic zinc ferrite ($ZnFe_2O_4$).

As shown in Fig. 2b), PDFMB mainly presents a nanorod structure. PANI nanofiber filaments are interlaced with each other, while Fe_3O_4 and $ZnFe_2O_4$ on PDFMB are basically invisible, indicating that the modified PANI is well dispersed on the DFMB surface. Most of the magnetic particles are embedded inside the PDFMB, while the interlaced fiber structure provides good load-type protection for the magnetic centers. PANI nanorods are distributed in a coral-like structure, and there are a large number of pores and channels on PDFMB, showing a rich mesoporous structure. This structure is conducive to the diffusion of Cr(VI) ions into the pores, and increases the contact probability between the adsorbent and adsorption sites [14]. Fig. 2c)

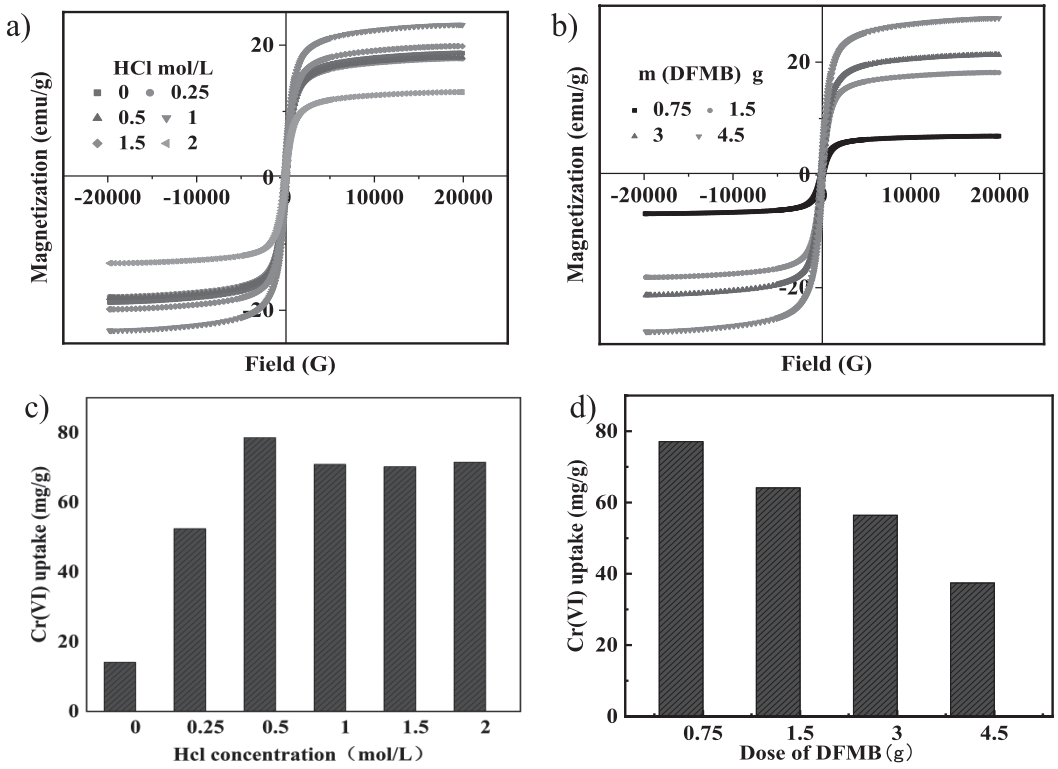


Fig. 1. a) VSM curves of PDFMB as a function of HCl concentration; b) VSM curves of PDFMB as a function of DFMB dosage; c) Cr(VI) removal of PDFMB as a function of HCl concentration; d) Cr(VI) removal of PDFMB as a function of DFMB dosage.

showed that the PANI nanofiber filaments and some of the pores were filled and covered with a layer of film, suggesting that Cr(VI) ions are adsorbed on the surface of PDFMB after adsorption.

Fig. 2d) and Fig. 2e) showed the N_2 adsorption-desorption isotherms of DFMB and PDFMB, which were classified as type IV isotherms. The DFMB isotherm had a type H_4 hysteresis loop, illustrating that the composite comprised micropores and mesopores. The PDFMB isotherm had an H_3 hysteresis loop, indicating that it had a layered structure with a mesoporous nature. As shown in Table 3, the BET specific surface area (S_{BET})

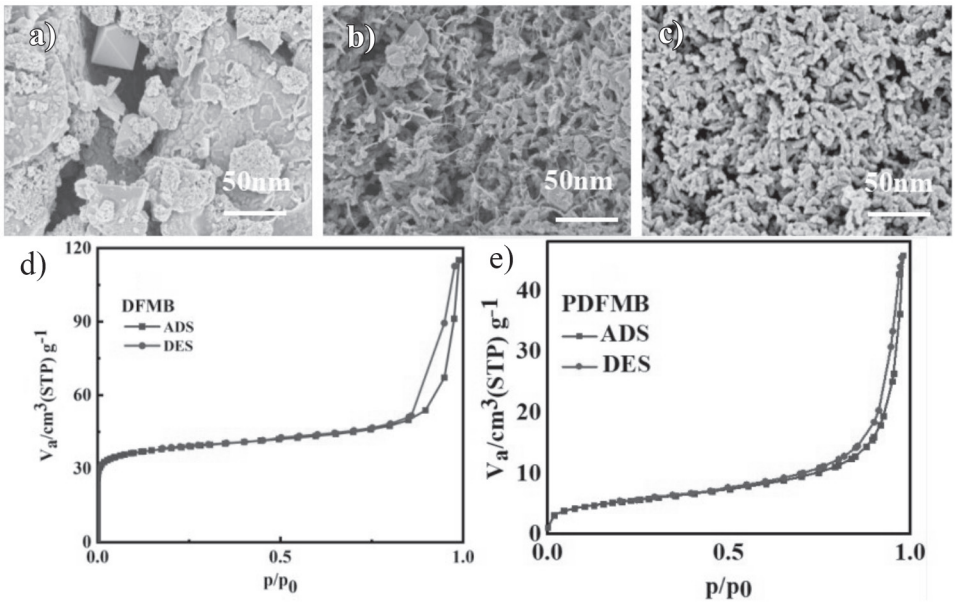


Fig. 2. SEM of a) DFMB, b) PDFMB and c) PDFMB after Cr(VI) adsorption; N_2 adsorption-desorption isotherms of d) DFMB and e) PDFMB.

Table 3. S_{BET} and pore textures of DFMB and PDFMB.

Adsorbent	S_{BET} (m^2/g)	Average pore diameter (nm)
DFMB	145.13	4.91
PDFMB	18.57	15.26

of DFMB and PDFMB were 145.13 m^2/g and 18.57 m^2/g, respectively. The average pore diameter increased from 4.91 nm to 15.26 nm after modification with PANI, showing that the micropores were blocked and abundant wedge-shaped mesopores were formed.

Combined with the morphological characteristics observed from SEM images, the BET results demonstrate an obvious structural trade-off originating from PANI coating modification. The mass-specific surface area contributed by the primitive micropores is kinetically unavailable to hydrated Cr(VI) oxyanions due to steric restrictions and severe diffusion barriers. Although PDFMB possesses a much lower total BET surface area, the opened mesoporous channels optimize the transmission pathways of Cr(VI) ions and greatly lower intraparticle diffusion resistance, enabling Cr(VI) to penetrate deep into the adsorbent interior and sufficiently contact internal active sites. Furthermore, the interlaced coral-shaped PANI nanorods introduce massive amine and imine functional groups with prominent specific chelation and reduction performance for Cr(VI). The loss of native surface adsorption sites is effectively compensated by these high-efficiency chemically active sites, achieving a favorable capacity compensation mode dominated by site quality rather than total surface quantity. The morphological feature in Fig. 2c), in which the pore channels are covered by adsorbed substances, also proves that Cr(VI) ions smoothly diffuse into the mesoporous structures and anchor on PANI active sites.

Adsorption Study

Effect of Initial Solution pH

The influence of initial aqueous pH on Cr(VI) adsorption by PDFMB was analyzed in an initial pH range of 2 to 10. Solution pH significantly affects the form of Cr(VI) in water and the functional groups on the surface of PDFMB. Fig. 3a) shows that the Cr(VI) uptake decreased from 155.26 mg/g to 49.50 mg/g as the pH increased from 2 to 10, indicating that a lower pH was favorable for the removal of Cr(VI) [15].

The pH_{PZC} (pH at the point of zero charge) is an important parameter that indicates the surface charge density of the material as a function of the aqueous solution pH [16]. When the solution pH was lower than pH_{PZC}, the functional groups on the material became protonated, and the surface of the material remained positively charged, promoting the electrostatic attraction to the anions in the solution. As shown in Fig. 3b), the zeta potential of PDFMB increased from -301.67 mV to 146.78 mV as the pH decreased from 10 to 2, and the pH_{PZC} of PDFMB was calculated to be 5.30. At pH<5.30, H^+ ions were abundant in the solution, and the functional groups on the surface of PDFMB were easily protonated, thus contributing to the electrostatic attraction toward the anions, including $HCrO_4^-$, CrO_4^{2-}, and $Cr_2O_7^{2-}$ (Fig. 3c). As the pH increased, deprotonation led to many negative charges on the surface of PDFMB, which caused the repulsion of anions. In addition, competition from OH^- continuously increased as the pH increased from 5.30 to 10, resulting in the weakening of Cr(VI) adsorption as well. The variation trend of the material surface charge derived from zeta potential measurements helps interpret some of the underlying reasons for the pH-dependent adsorption discrepancy of Cr(VI).

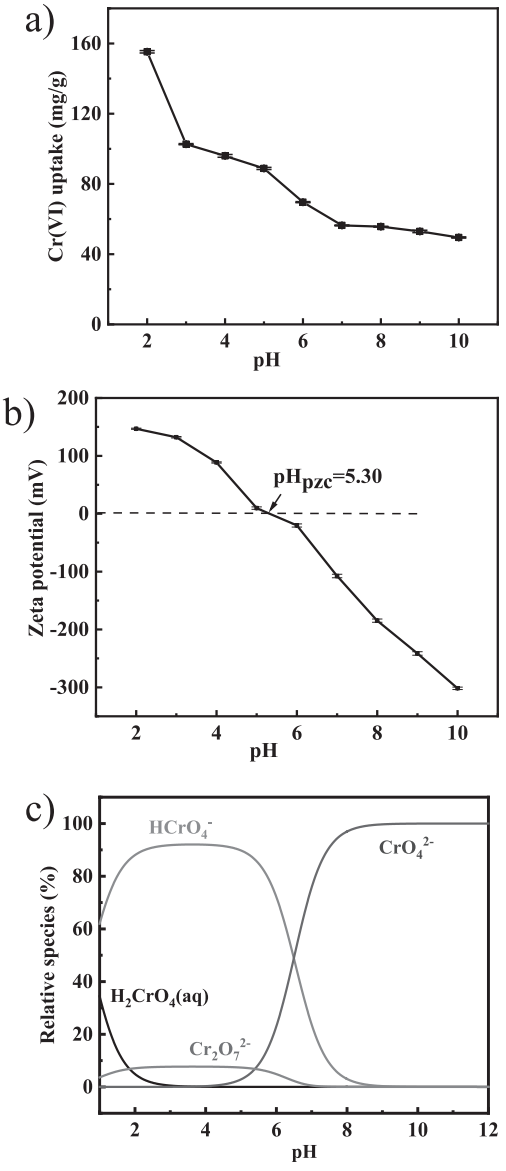


Fig. 3. a) Cr(VI) adsorption at a series of initial pH values (C_0 = 500 mg/L, time = 6 h, T = 25°C); b) Zeta potential of PDFMB; c) existing forms of Cr(VI) in solution at different pH.

Effect of Adsorption Time and Adsorption Kinetics

Fig. 4a) showed that the Cr(VI) uptake increased gradually with increasing reaction time, and the whole process had two distinct stages. Due to the abundant active sites on the surface of PDFMB, Cr(VI) adsorption occurred rather quickly in the first stage. At the three initial concentrations, the removal rate of Cr(VI) ions exceeded 50% when the adsorption reaction was carried out for 30 min. Compared with the equilibrium adsorption uptake, the adsorption uptake rapidly reached 89.9%, 81.3%, and 80.6% within the first 6 h for the initial Cr(VI) concentrations of 100, 150, and 200 mg/L. The Cr(VI) adsorption by PDFMB showed a slow growth trend in the second stage and reached equilibrium at 12 h, 16 h, and 18 h under the three initial concentrations, respectively.

The pseudo-first-order (PFO) model [17] and pseudo-second-order (PSO) model [18] were used to analyze the adsorption kinetics. The linear kinetic plots of the two models are shown in Fig. 4b) and Fig. 4c), and the kinetic parameters are listed in Table 4. The three coefficients (R^2) of the PSO model at different initial concentrations of Cr(VI) were 0.9997, 0.9978, and 0.9988, which were higher than those of the PFO model. For the initial Cr(VI) concentrations of 100, 150, and 200 mg/L, the Cr(VI) adsorption capacities_calculated with the PSO model were 52.44, 76.80, and 90.83 mg/g, respectively, which agreed with the experimental values of 51.90, 76.21, and 89.52 mg/g. Therefore, the PSO model was more suitable for representing Cr(VI) adsorption by PDFMB, illustrating that the adsorption process was mainly affected by chemical reactions.

Adsorption Isotherms

At 10, 25, and 35°C, the adsorption capacity of PDFMB increased from 39.42 to 93.14 mg/g, from

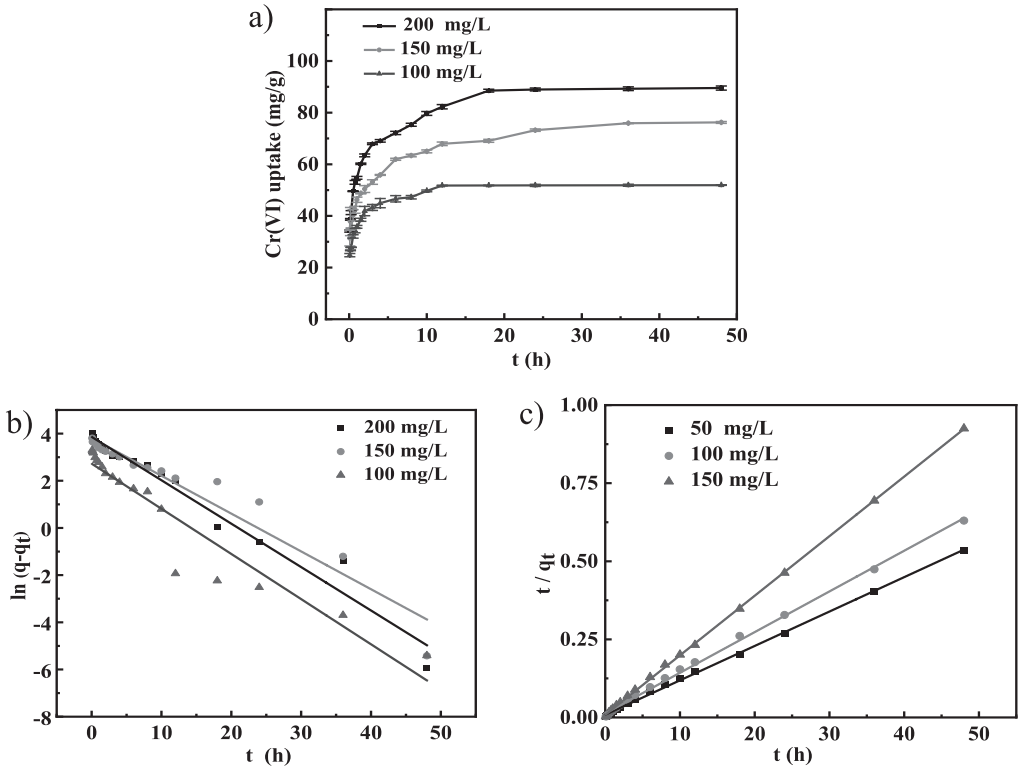


Fig. 4. a) Effect of reaction time on Cr(VI) adsorption (C_0 = 100, 150, and 200 mg/L, pH = 5, T = 25°C); linear fitting plot of b) pseudo-first-order model and c) pseudo-second-order model.

Table 4. The parameters for the adsorption kinetics.

C_0 mg/L	pseudo-first-order			pseudo-second-order		
	Q_e mg/g	k_1 h^{-1}	R^2	Q_e mg/g	k_2 g/(mg·h)	R^2
100	15.29	0.1915	0.9086	52.44	0.0190	0.9997
150	45.31	0.1603	0.9299	76.80	0.0130	0.9978
200	47.56	0.1840	0.9654	90.83	0.0110	0.9988

39.95 to 104.96 mg/g, and from 39.91 to 109.59 mg/g with increasing initial concentrations of Cr(VI) (Fig. 5a)). The promotion of Cr(VI) adsorption can be attributed to the improvement in the mass transfer rate. The concentration difference between the solution and the adsorbent increased clearly as the initial Cr(VI) concentration increased, and hence the adsorption capacity increased gradually.

The Freundlich model [19] and Langmuir model [20] were used to describe the adsorption isotherm. The linear kinetic plots of the two models are shown in Fig. 5b) and Fig. 5c), and Table 5 shows the isotherm parameters for the adsorption. The regression coefficient (R^2>0.995) of the Langmuir model was higher than that of the Freundlich model at all temperatures. The Langmuir model was more appropriate for describing the adsorption process, indicating that the adsorption of Cr(VI) by PDFMB had a monolayer adsorption nature. The maximum Cr(VI) uptakes calculated by the Langmuir isotherm model were 96.25, 105.00, and 111.11 mg/g at 10, 25, and 35°C, respectively.

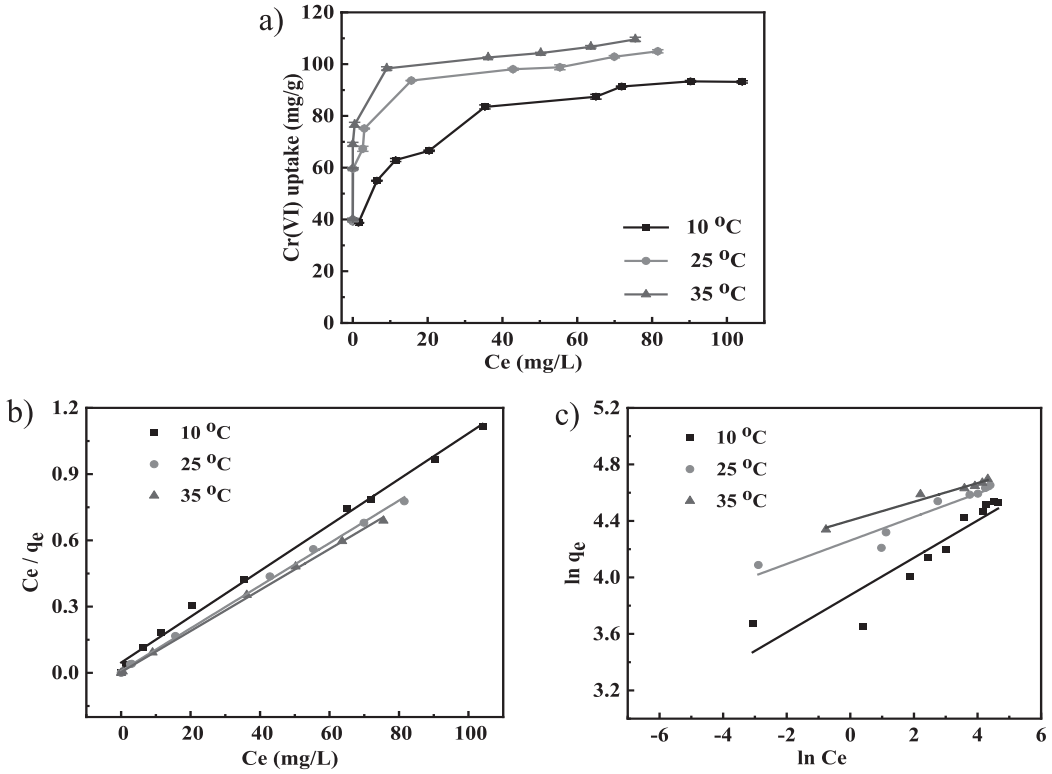


Fig. 5. a) Cr(VI) adsorption isotherms (T = 10, 25, and 35°C, pH = 5, time = 24 h); b) Langmuir and c) Freundlich fitting results.

Table 5. The parameters of the adsorption isotherms.

Reaction Temperature °C	Langmuir				Freundlich		
	Q_m mg/g	K_L L/mg	R^2	R_L	K_f	1/n	R^2
10	96.25	0.224	0.9952	0.015	48.192	0.1319	0.8502
25	105.00	1.092	0.9985	0.003	70.921	0.0831	0.9167
35	111.11	2.679	0.9990	0.001	81.691	0.0663	0.9744

Table 6. The parameters of the thermodynamic constants.

Reaction Temperature	ΔG^0 (KJ/mol)	ΔH^0 (KJ/mol)	ΔS^0 (J/mol·K)
283 K	-2.13	14.92	60.25
298 K	-3.03		
308 K	-3.64		

The thermodynamic characteristics of Cr(VI) adsorption onto PDFMB were investigated at 283 K, 298 K and 308 K [21], with the calculated thermodynamic parameters summarized in Table 6. All ΔG^0 values were negative and became more negative with increasing temperature (-2.13 kJ/mol at 283 K, -3.03 kJ/mol at 298 K, -3.64 kJ/mol at 308 K), which confirms that the Cr(VI) adsorption process was spontaneous and that the spontaneous tendency was strengthened at elevated temperatures. The positive enthalpy change (ΔH^0 = 14.92 kJ/mol) demonstrates the intrinsic endothermic property of this adsorption system. Meanwhile, the positive entropy value (ΔS^0 = 60.25 J/(mol·K)) suggests an increase in the randomness of the solid–liquid interfacial system during Cr(VI) capture by PDFMB.

Effect of Coexisting Ions

The impacts of coexisting ions on Cr(VI) removal by PDFMB were studied, and the findings are given in Fig. 6a) and Fig. 6b). In comparison, the influence was not noticeable except for SO_4^{2-} and PO_4^{3-}. The major reason for the competition might be the similar ionic nature of the anions and Cr(VI). Fig. 6b showed that the order of negative effects followed $Cl^- < SO_4^{2-} < PO_4^{3-}$, indicating that the interference was closely related to the charge of the anions. In addition, the inhibitory effect on Cr(VI) adsorption was enhanced as the anion concentration increased. When the concentration of PO_4^{3-} was 0.01, 0.05, and 0.1 mol/L, respectively, the adsorption capacity of Cr(VI) dropped to 75.81, 68.16, and 62.43 mg/g, causing decreases of 8.19%, 17.46%, and 24.39%.

Effect of Coexisting Contaminants

Anionic Congo red (CR), cationic Rhodamine B (RhB), and Cr(VI) were selected as target contaminants. Adsorption experiments were performed to investigate the removal performance of PDFMB toward the three pollutants in single-component and mixed aqueous systems, with the initial dye concentration fixed at 100 mg/L and the initial Cr(VI) concentration set to 500 mg/L. The corresponding results are displayed in Fig. 7.

PDFMB exhibited higher adsorption capacities for anionic CR and Cr(VI) than for cationic RhB in single-pollutant systems. This phenomenon was attributed to the point of zero charge (pH_{PZC}) of PDFMB at 5.30. The material surface was positively charged at pH<5.30, generating strong electrostatic attraction toward anionic pollutants. In the CR-Cr(VI) binary coexisting system, competitive adsorption occurred between the two anionic species. Nevertheless, abundant positively charged nitrogen-containing functional groups were distributed on the PDFMB surface. The adsorption capacities of CR and Cr(VI) were only slightly reduced, with negligible mutual inhibitory effects, verifying the reliable decontamination capacity of PDFMB toward CR and Cr(VI) under coexisting conditions.

For the RhB-Cr(VI) mixed system, intensified electrostatic interactions existed among RhB, Cr(VI), and PDFMB. Synchronous oxidative degradation of RhB and reductive conversion of Cr(VI) accelerated interfacial electron transfer, thereby producing a synergistic promotion effect on the uptake of both pollutants. Collectively, PDFMB possessed favorable structural stability and outstanding adsorption capability, enabling efficient simultaneous removal of multiple pollutants in complex coexisting wastewater matrices.

PDFMB Recycling

After saturation adsorption of Cr(VI), the spent PDFMB was regenerated. Specifically, a 0.5 mol/L NaOH solution, as a desorbing eluent [22], was mixed with the spent PDFMB for 3 h at 25°C. The regenerated PDFMB was reactivated with 80 mL of 0.1 mol/L HCl solution for 2 h at 25°C. The product was rinsed repeatedly with deionized water and dried in a vacuum oven. The regeneration was repeated 6 times.

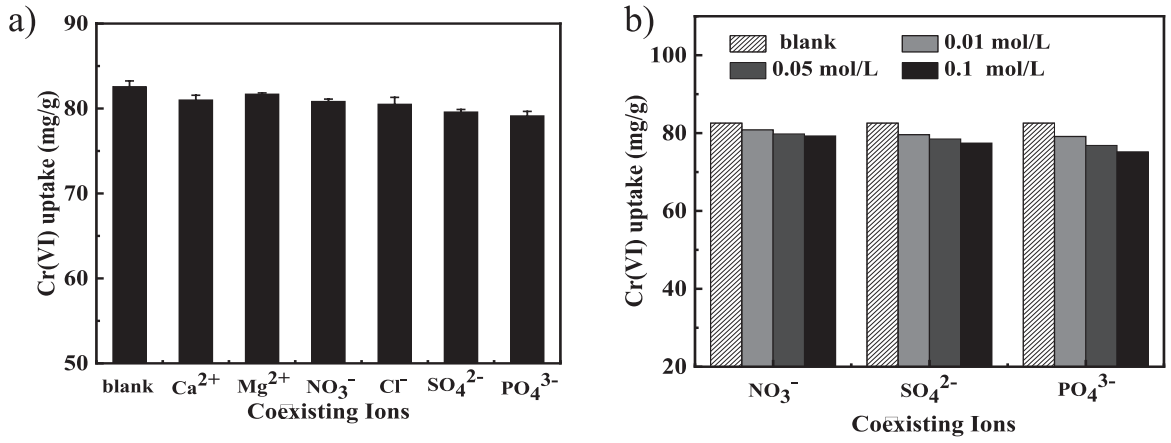


Fig. 6. Effect of co-existing ions with different a) kinds and b) concentrations (C_0 = 120 mg/L, time = 6 h, pH = 5, T = 25°C).

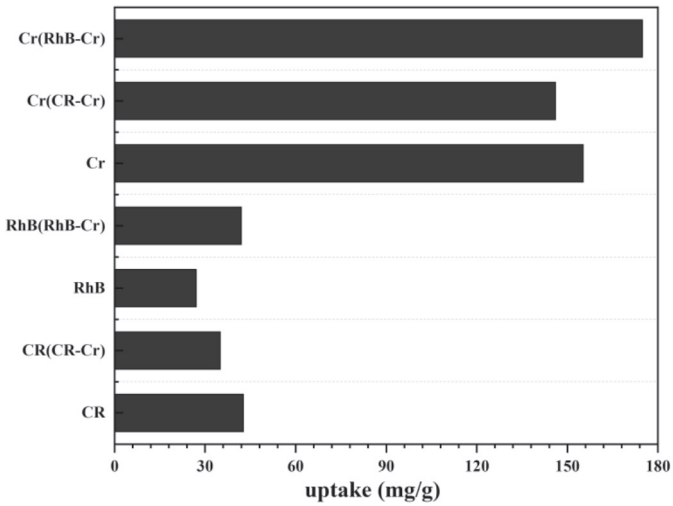


Fig. 7. Effect of coexisting contaminants (time = 6 h, pH = 5, T = 25°C).

A regeneration experiment was conducted to analyze the reusability potential of PDFMB. As shown in Fig. 8a), the Cr(VI) uptake of the raw PDFMB was 81.47 mg/g. Compared with the raw PDFMB, the Cr(VI) uptake decreased by 3.87% after the first regeneration. After six regeneration cycles, the Cr(VI) uptake was still 69.45 mg/g, representing a decrease of 14.75%. As illustrated in the SEM images of PDFMB after regeneration cycles (Fig. 8b), the material surface was partially covered by chromium species after Cr(VI) adsorption. After 6 regeneration treatments, the overall morphology of regenerated PDFMB did not change significantly. The complete carbon skeleton and distinct nanorod structures were well preserved, demonstrating the favorable structural stability of PDFMB and confirming that the adsorbent could be effectively recovered via desorption treatment. Zhao et al. [23] synthesized CMC-AM for Cr(VI), and the results showed that 86% of Cr^{6+} ions were still removed after six cycles. Masuku et al. [24] fabricated pinecone biochar and studied adsorbent regeneration and reusability, with the adsorbent retaining a 50% removal efficiency over 3 regeneration cycles. By comparison, the as-prepared PDFMB in this study retained 85.25% of its initial Cr(VI) adsorption capacity after six cycles, indicating its excellent regeneration performance.

Comparative Evaluation of PDFMB against Various Adsorbent Materials

Pristine biochar exhibits poor adsorption performance for heavy metals, and further modification is required to improve its adsorption capacity. Table 7 summarizes the Cr(VI) adsorption capacities of various adsorbents in this study and those reported in previous literature, which were calculated based on the Langmuir model. Among the 18 listed adsorbents, PDFMB delivers a high Cr(VI) adsorption capacity and excellent magnetic properties, demonstrating its great potential for Cr(VI) removal from aqueous solutions.

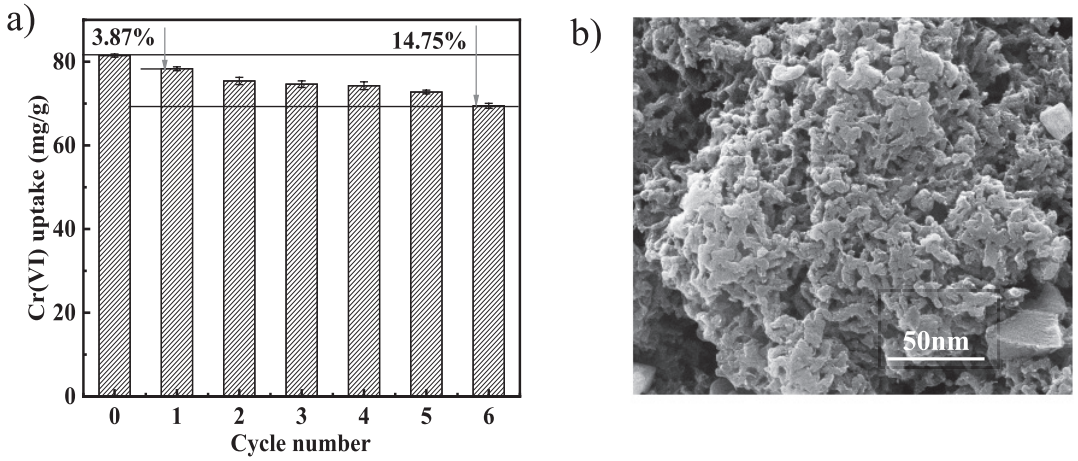


Fig. 8. a) The reusability study of PDFMB (C_0 = 250 mg/L, pH = 5); b) SEM image of PDFMB after regeneration cycles.

Table 7. Comparison of monolayer Cr(VI) adsorption capacities of various adsorbents.

Adsorbents	Moments (emu/g)	q_m (mg/g)	Conditions (K and pH)	Reference
Iron-modified chitosan/coconut shell activated carbon	-	58.04 63.41 64.49	298 and 3 308 and 3 318 and 3	[25]
PANI@Nd-LDH	-	219	298 and 3	[26]
CFA/GO/PANI nanocomposite	-	124.72	298 and 2	[27]
Cit-nZVI@BC	-	187.5	298 and 3	[28]
BC-nZVI@Cell-g-PAA	-	69.54	298 and 3	[29]
chitosan-allophane nanocomposite	-	112.17	298 and 3	[30]
Microwave-assisted hydrothermal carbonization of furfural residue	-	78.08	298 and 2	[31]
MNP/SBACC	2.35	80.21	298 and 2	[32]
Mag-PAC	9.66	75.76	298 and 2	[33]
Ppy@MNCFB	3.6	111.11	328 and 7	[34]
Magnetic zeolite/chitosan composites	18.67	28.47	303 and 3	[35]
nZVI@PEI/EVMT	41.5	116.2	303 and 2	[36]
FCN-500	54.3	52.63	308 and 3	[37]
MBC	5.44	25.62	303 and 2	[38]
PMGO	12.4	148.98	313 and 3	[39]
MABN	11.11	95.16	303 and 2	[40]
PDFMB	18.13	96.25 105.00 111.11 170.65	283 and 5 298 and 5 308 and 5 308 and 2	Current study

The "-" in the table indicates that this parameter was not explicitly specified in the study.

The adsorption performance of Cr(VI) is generally strongly dependent on solution pH, and higher adsorption capacities are commonly obtained under acidic conditions. Zhou et al. [28] prepared Cit-nZVI@BC, which achieved an adsorption capacity of 187.5 mg/g at pH 3. Yang et al. [36] synthesized nZVI@PEI/EVMT with an adsorption capacity of 116.2 mg/g at pH 2. Saeed et al. [40] fabricated PMGO, which exhibited an adsorption capacity of 148.98 mg/g at pH 3. The high Cr(VI) uptake of these 3 materials was achieved under acidic conditions. Notably, PDFMB reaches an outstanding adsorption capacity of 170.65 mg/g at pH 2, ranking among the highest values across the 15 compared adsorbents. Even at pH 5, its Cr(VI) adsorption capacity remains as high as 111.11 mg/g, proving that the as-prepared materialpossesses favorable adsorption performance over a wide pH range.

CFA/GO/PANI nanocomposites synthesized by Umejuru et al. [27] and chitosan-allophane nanocomposites prepared by Pazoki et al. had Cr(VI) adsorption capacities of 124 mg/g and 112 mg/g, respectively. However, these materials lack magnetism and thus cannot be regenerated or reused. MNP/SBACC developed by Ramya et al., Mag-PAC by Sangkarak et al., and Ppy@MNCFB by Samal et al. [34] exhibited weak magnetism (2-10 emu/g), with corresponding adsorption capacities of 80.21 mg/g, 75.76 mg/g, and 111.11 mg/g. Magnetic zeolite/chitosan composites fabricated by Liu et al. [35] and FCN-500 synthesized by Juturu et al. [38] showed strong magnetism of 18.67 emu/g and 54.3 emu/g, respectively, whereas their adsorption capacities were relatively low at 28.47 mg/g and 52.63 mg/g. These findings reveal that magnetic modification usually reduces the adsorption capacity of adsorbents. In comparison, PDFMB possesses satisfactory magnetism (18.13 emu/g) while maintaining high adsorption efficiency, with a Cr(VI) uptake of 170.65 mg/g at pH 2. The superior magnetism enables rapid separation of PDFMB from wastewater, facilitating its regeneration and cyclic utilization.

Notably, PDFMB in this work was fabricated using solid wastes as raw materials, resulting in low cost and environmental friendliness. Combined with its high Cr(VI) adsorption capacity, excellent pH adaptability and desirable magnetic properties, the as-synthesized PDFMB exhibited outstanding comprehensive performance and promising application prospects for

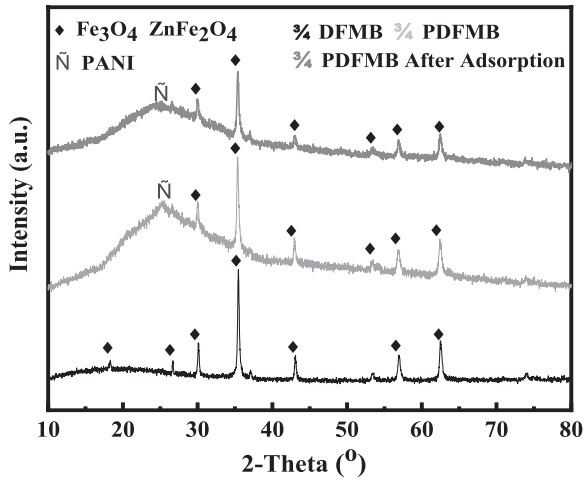


Fig. 9. XRD patterns of DFMB, PDFMB, and PDFMB after Cr(VI) adsorption.

Cr(VI) removal from wastewater.

Exploration of the Adsorption Mechanism

The XRD, FTIR, and XPS characterization results were jointly analyzed and cross-verified to systematically clarify the integrated reaction pathway of Cr(VI) removal by PDFMB.

XRD Analysis

The structures and crystallinities of DFMB, PDFMB, and PDFMB after Cr(VI) adsorption were studied by XRD, and the findings are shown in Fig. 9. The main characteristic peaks at 2θ values of 30.08º, 35.43º, 43.05º, 53.41º, 56.94º and 62.52º were attributed to the (220), (311), (400), (422), (511) and (440) crystal planes of $ZnFe_2O_4$ (JPCDS No.1-1109) and Fe_3O_4 (JPCDS No.19-0629) [41, 42]. The XRD patterns of PDFMB showed a broad peak at 25º, which was ascribed to periodic parallel and perpendicular PANI chains in the semicrystalline structure [43]. Hence, the ferromagnetic material and PANI were successfully combined by a one-pot technique, which was consistent with the SEM and VSM analyses. In addition, the characteristic peaks of PDFMB distinctly decreased at 2θ = 25º, 30.08º, 35.43º, 43.05º, 56.94º and 62.52º after Cr(VI) adsorption. This peak attenuation preliminarily proves that abundant surface functional groups on the composite participate in Cr(VI) sequestration, which is further corroborated by subsequent FTIR functional group shifts and XPS surface elemental variations.

FTIR Analysis

FTIR spectra further track functional group evolution before and after Cr(VI) adsorption to supplement the structural clues from XRD (Fig. 10). The wide peak at 3443 cm^{-1} was assigned to O-H [44]. The peak at 2919 cm^{-1} was attributed to the C-H [45]. The characteristic stretching vibrations located at 1574 and 1471 cm^{-1} were related to the C=C of quinoid rings and C=C of benzenoid rings [46 ,47], while the peaks at 1295, 1235, and 1108 cm^{-1} were assigned to the C–N, $C–N^+$ and $=N^+–H$ stretching vibrations, respectively. These characteristic peaks are typical of PANI in the emeraldine salt state. Two adsorption peaks at 558 and 493 cm^{-1} were assigned to the stretching vibrations of Fe-O and Zn-O [48, 49], illustrating that Fe_3O_4 and $ZnFe_2O_4$ were present. After Cr(VI) adsorption, the O-H peak became broader at 3396 cm^{-1}, while the peak at 2919 cm^{-1} disappeared. The peaks at 1574, 1471, 1295, 1235, and 1108 cm^{-1} shifted to 1581, 1497, 1380, 1314, and 1150 cm^{-1}, respectively. In addition, the peaks at 558 and 493 cm^{-1} shifted to a strong peak at 526 cm^{-1}. These FTIR spectral shifts demonstrate strong chemical interactions between Cr species and surface -OH, PANI amine groups, and metal-oxide sites, consistent with XRD peak fading; XPS high-resolution spectra further

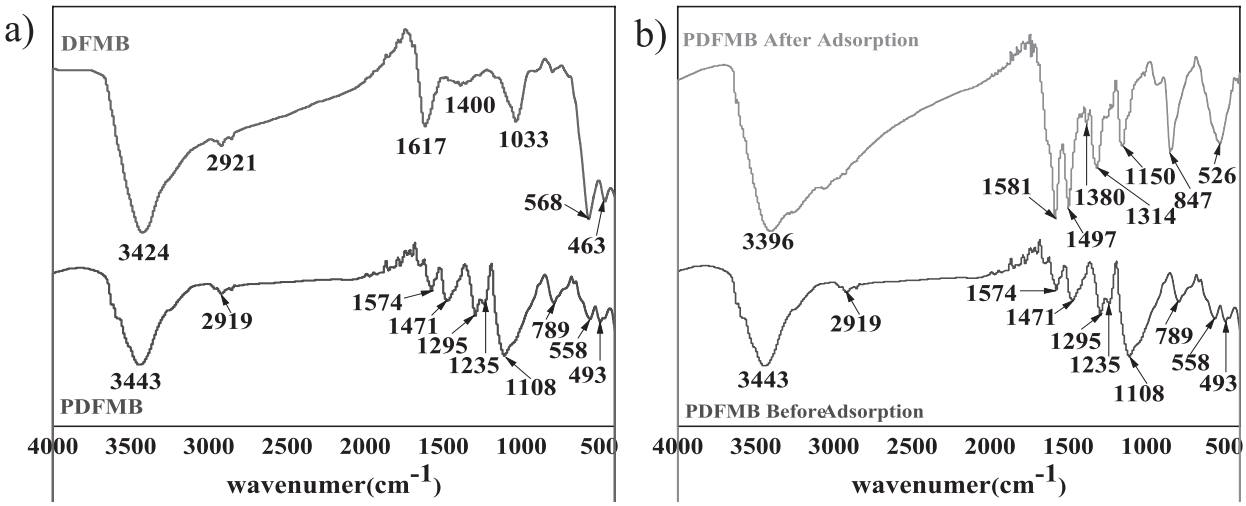


Fig. 10. a) FTIR spectra of DFMB and PDFMB; b) FTIR spectra of PDFMB before and after adsorption.

quantify valence and elemental changes induced by these chemical interactions.

XPS Analysis

XPS survey and high-resolution spectra quantitatively reveal surface elemental composition, chemical valence and binding state changes, cross-verifying the redox and complexation processes inferred from XRD and FTIR (Fig. 11). The XPS spectrum of DFMB revealed the presence of Fe and Zn (Fig. 11a)). N appeared in the XPS spectrum after modification with PANI, while the peaks of Fe and Zn were weakened, indicating that PANI was successfully loaded onto the surface to form a magnetic core-shell structure. Fig. 11a) showed that a Cr peak appeared after Cr(VI) adsorption, indicating that Cr(VI) was adsorbed onto the surface of PDFMB.

Fig. 11b) shows that the O 1s spectra contained two peaks at 530.13 and 532.39 eV, which were attributed to -OH and C=O, respectively [50]. The two peaks were shifted to 530.22 and 531.15 eV, respectively, after Cr(VI) adsorption, indicating that the interaction between Cr(VI) and oxygen functional groups in PDFMB may have formed new chemical bonds, which can be described by Eq. (1).

As shown in Fig. 11c), C=C and C=N had peaks at approximately 284.48 and 288.42 eV [51], while the peak at 285.18 eV corresponded to C-N^+ and C=N^+ [52], indicating the presence of PANI. After Cr(VI) adsorption, the peak area of C-N^+/C=N^+ decreased from 54.75% to 35.94%, while the peak area of C=C increased from 30.55% to 53.91%. This depletion of protonated nitrogen sites aligns with the FTIR nitrogen band shifts, indicating that protonated PANI sites consume electrons and participate in Cr(VI) binding and reduction.

As shown in Fig. 11d), the N 1s spectrum can be divided into three peaks, which were assigned to quinone imine (–N=, 398.55 eV), secondary amine (–NH–, 399.26 eV) and positively charged imine nitrogen (–N^+=, 400.12 eV) [53-56]. The peak area of –NH– decreased from 51.77% to 46.54%, and the –NH– peak shifted to a higher binding energy, indicating that the –NH– group acted as an electron donor during adsorption to reduce Cr(VI) to Cr(III). The proportion of -N= increased from 9.85% to 22.43% after adsorption, indicating a redox reaction occurred between PANI and Cr(VI) [57, 58], and the –N= group served as a binding site for complexed Cr(III). Reduced proportions of –N^+= and –NH– jointly confirm electrostatic attraction as the initial driving force for capturing anionic Cr(VI) oxyanions, consistent with FTIR peak shifts of amine functional groups (Eqs. (2)-(5)).

The Fe 2p spectrum is shown in Fig. 11e). Two peaks at 713.13 eV and 726.69 eV belong to Fe 2p3/2 and Fe 2p1/2 of Fe(III), respectively [59]. Two peaks at 711.01 eV and 724.27 eV corresponded to Fe 2p3/2 and Fe 2p1/2 of Fe(II), and a satellite peak of Fe(II) emerged at 719.25 eV [60]. The peaks attributed to both Fe(III) and Fe(II) shifted after Cr(VI) adsorption. Meanwhile, the peak region for Fe(III) increased from 37.73% to 53.15%, while the peak area of Fe(II) declined from 62.27% to 46.85%. This valence conversion confirms that Fe(II) serves as the second reducing component for Cr(VI) reduction [61]. The resulting Cr^{3+} combines with Fe^{3+} and surface hydroxyl groups to form mixed hydroxide precipitates (Eqs. (6)-(8)). This valence evolution process is consistent with the characterization results: the original split Fe-O/Zn-O vibration peaks merge into one broad peak in FTIR, and the diffraction intensities of metal ferrites decrease significantly in XRD.

As shown in Fig. 11f), Cr was adsorbed on the surface of PDFMB. The peaks at 576.8 and 586.4 eV corresponded to Cr 2p3/2 and Cr 2p1/2 of Cr(VI), respectively, and accounted for 41.69% of the total peak area. Peaks at 576.52 eV and 586.11 eV were assigned to Cr 2p3/2 and Cr 2p1/2 of Cr(III), respectively, and their peak areas increased from 0 to 58.31% after Cr(VI) adsorption. The Cr 2p results provide direct evidence for the chemical precipitation pathway, supported by O 1s peak shifts in XPS, broadened hydroxyl bands in FTIR, and weakened crystal diffraction in XRD.

$$\text{-OH}+Cr^{3+}\rightarrow Cr(OH)_3 \quad (1)$$

$$HCrO_4^-+3PANI^0+7H^+\rightarrow Cr^{3+}+3PANI^++4H_2O \quad (2)$$

$$Cr_2O_7^{2-}+6PANI^0+14H^+\rightarrow 2Cr^{3+}+6PANI^++7H_2O \quad (3)$$

$$\text{-}NH^+\text{-}+HCrO_4^-\rightarrow \text{-}NH^+\cdots HCrO_4^- \quad (4)$$

$$\text{-}NH^+\text{-}+Cr_2O_7^{2-}\rightarrow \text{-}NH^+\cdots Cr_2O_7^{2-} \quad (5)$$

$$3Fe^{2+}+HCrO_4^-+7H^+\rightarrow 3Fe^{3+}+Cr^{3+}+4H_2O \quad (6)$$

$$3Fe^{2+}+CrO_4^{2-}+8H^+\rightarrow 3Fe^{3+}+Cr^{3+}+4H_2O \quad (7)$$

$$Fe^{3+}+Cr^{3+}+H_2O\rightarrow Cr_xFe_{1-x}(OH)_3+3H^+ \quad (8)$$

Cross-comparison of the evolution of the XRD crystal structure, variation in FTIR functional groups, and transformation of XPS surface elemental valence states revealed the synergistic reaction pathways involved in Cr(VI) removal by PDFMB. Positively charged protonated amino groups on polyaniline chains can capture negatively charged chromate and dichromate anions through electrostatic attraction, as evidenced by obvious shifts in nitrogen-related FTIR absorption bands and a decreased proportion of protonated nitrogen species in the N 1s spectra. Moreover, ferrous ions act as reducing components to convert adsorbed toxic Cr(VI) into Cr(III). The in situ-generated Cr^{3+} can chelate with surface hydroxyl groups and coprecipitate with Fe^{3+} to form stable insoluble $Cr_xFe_{1-x}(OH)_3$ precipitates, which corresponds to the

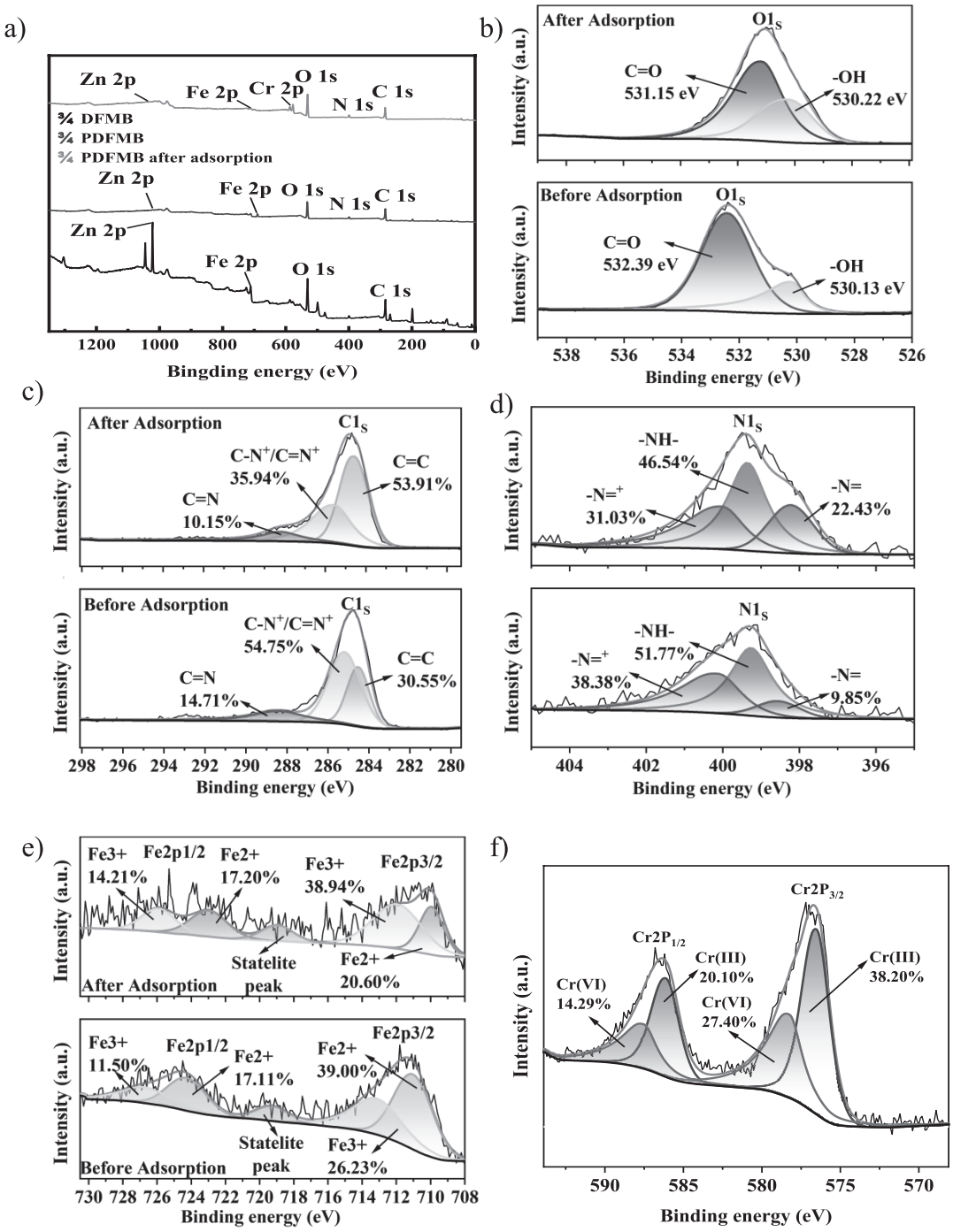


Fig. 11. a) XPS spectra of DFMB and PDFMB before and after adsorption; b) detailed survey of O 1s; c) C 1s; d) N 1s; e) Fe 2p; f) Cr 2p before and after Cr(VI) adsorption by PDFMB.

overall attenuation of all XRD characteristic peaks and the merging of metal oxide vibration bands in FTIR spectra.

In summary, the experimental findings verified that PDFMB possessed outstanding capability for high-efficiency Cr(VI) removal. Combined with the cross-validated spectroscopic characterization results described above, the Cr(VI) immobilization process was governed by multiple synergistic reactions (the corresponding reaction mechanism is displayed in Fig. 12), which mainly consist of physical and chemical electrostatic adsorption, surface chelation, and the redox transformation of toxic Cr(VI) into less hazardous Cr(III) species.

Conclusions

This study aimed to achieve resource recovery from solid waste and the removal of Cr(VI) from water. To this end, iron-based sludge and Chinese medicine residue were utilized as raw materials, with zinc ions

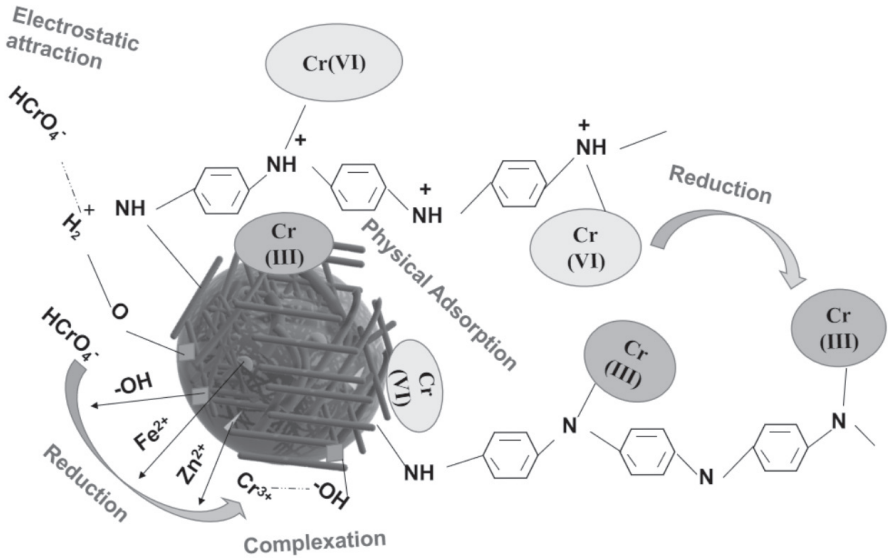


Fig. 12. Schematic illustration of the reaction mechanism.

and polyaniline incorporated as modifiers, to develop a magnetic biochar material (PDFMB) for the adsorption and removal of Cr(VI) from aqueous solutions. The adsorption behavior of PDFMB was strongly pH-dependent, with acidic conditions significantly promoting Cr(VI) removal, and the maximum monolayer adsorption capacity was 111.11 mg/g at 308 K and pH 5. The adsorption process conformed to the pseudo-second-order kinetic and Langmuir isotherm models, while thermodynamic analysis confirmed the spontaneous and endothermic nature of the adsorption process. PDFMB retained 85.25% of its initial adsorption performance after six regeneration cycles, demonstrating considerable potential for heavy metal wastewater treatment. A comprehensive assessment of the adsorption experiments and material characterization results demonstrated that PDFMB can effectively remove Cr(VI) from wastewater, with adsorption driven primarily by electrostatic physical and chemical adsorption, surface chelation, and redox transformation.

Although batch static experiments verified the favorable Cr(VI) removal performance of PDFMB, this study still has obvious limitations for practical engineering applications. The dynamic adsorption stability and stacking effects of PDFMB under continuous flow conditions remain unclear, which substantially restricts its large-scale engineering promotion and application. To address these deficiencies and further promote the practical application of PDFMB, further targeted research is needed. First, continuous column adsorption tests should be conducted to investigate the dynamic adsorption performance under different flow rates and filler conditions, thereby providing basic parameters for practical reactor design. Second, toxicity leaching tests of saturated and regenerated PDFMB should be conducted to evaluate secondary pollution risks and verify its environmental safety. Third, a systematic economic analysis covering raw material preparation, energy consumption, and regeneration costs should be performed, to clarify the economic competitiveness of PDFMB through comparison with traditional adsorbents. Additionally, systematic mixed-ion interference experiments and pilot-scale actual wastewater treatment tests should be conducted in subsequent research to further verify the engineering applicability of the PDFMB adsorbent. These follow-up studies will effectively provide additional engineering application data of PDFMB and facilitate the industrialization of this solid waste-based adsorbent for Cr(VI)-containing wastewater treatment.

Acknowledgments

This research was funded by the 2025 Henan Province Science and Technology Research and Development project (252102210090, 252102211032), the 2026 Henan Province Science and Technology Research and Development project (262102321038, 262102320117), and the General Project of Education Science Planning in Henan Province (2025YB0109, 2025YB0452).

Conflict of Interest

The authors declare no conflict of interest.

References

1. PRATAP B., KUMAR S., NAND S., AZAD I., BHARAGAVA R.N., FERREIRA L.F.R., DUTTA V. Wastewater generation and treatment by various eco-friendly technologies: Possible health hazards and further

reuse for environmental safety. Chemosphere, **313**, 137547, **2023**.
2. GIURLANI W., PAPPAIANNI G., BIFFOLI F., MARIANI E., BONECHI M., GILIBERTI L., TUFARELLI M., FRANZO P., CIANFANELLI E., INNOCENTI M. What Is the Current State of Sustainability in the Decorative Electroplating Industry? A Close Look at New Practices and Advances. Sustainability, **16** (13), 5821, **2024**.
3. MALLIK A.K., MOKTADIR M.A., RAHMAN M.A., SHAHRUZZAMAN M., RAHMAN M.M. Progress in surface-modified silicas for Cr (VI) adsorption: A review. Journal of Hazardous Materials, **423**, 127041, **2022**.
4. WANG R., ZHENG X., FENG Z., FENG Y., YING Z., WANG B., DOU B. Hydrothermal carbonization of Chinese medicine residues: Formation of humic acids and combustion performance of extracted hydrochar. Science of The Total Environment, **925**, 171792, **2024**.
5. YUAN J., WANG C., TANG Z., CHU T., ZHENG C., HAN Q., CHEN H.L., TAN Y. Biochar derived from traditional Chinese medicine residues: An efficient adsorbent for heavy metal Pb (II). Arabian Journal of Chemistry, **17** (3), 105606, **2024**.
6. YAZDANDOOST Z., ZONOOZI M.H. Treatment of oil-water emulsion through coagulation-flocculation and sedimentation using waterworks sludge as a green agent. Journal of Environmental Chemical Engineering, **13** (3), 116548, **2025**.
7. ZHAO X., HU J., YANG Y., LIU M., WANG H. Enhanced Cr (VI) removal from water by Fe-modified sewage sludge biochar: Influencing factors and mechanisms. Journal of Environmental Chemical Engineering, **13** (5), 117501, **2025**.
8. KHAN A., HUO Y., QU Z., LIU Y., WANG Z., CHEN Y., HUO M. A facile calcination conversion of groundwater treatment sludge (GTS) as magnetic adsorbent for oxytetracycline adsorption. Scientific Reports, **11** (1), 5276, **2021**.
9. MAITI P., MANGSATABAM M., CHATTERJEE A., SIDDIQI H., MISHRA A., MEIKAP B.C. In-situ synthesis of efficient $ZnCl_2$ doped pyrolyzed biochar for adsorptive remediation of organic dyes: performance evaluation, mass transfer and mechanism. Separation and Purification Technology, **329**, 125096, **2024**.
10. MI X., WANG T., CHEN Y., CAO D., MA N., DAI W. Ingenious construction of a magnetic-recyclable photo-Fenton catalyst $ZnFe_2O_4$@ MIL-88A (Fe) and its adsorption-degradation activity toward levofloxacin. Journal of Environmental Sciences, **151**, 677, **2025**.
11. SAMADI A., WANG Z., WANG S., NATARAJ S. K., KONG L., ZHAO S. Polyaniline-based adsorbents for water treatment: Roles of low-cost materials and 2D materials. Chemical Engineering Journal, **478**, 147506, **2023**.
12. MAO Z., WU D., SARKODIE B., SHI J., TAO Y., WANG D., ZHAO L., CAO A., ZHANG J. FENG Q. Scalable, acid-resistant polyaniline deposited amidoxime PAN nanofibers for efficient adsorption and detoxification of Cr (VI) wastewater. Journal of Environmental Chemical Engineering, **12** (5), 113153, **2024**.
13. BEHERA A., SAHU S., PAHI S., PATEL R.K. Flower‐Like Polyaniline‐Modified Yttrium Phosphate Nanocomposite: An Effective Adsorbent for Cr (VI) Removal via Adsorption‐Reduction Mechanism. Advanced Engineering Materials, **27** (20), 2500296, **2025**.
14. MA J., REN H., LIU Z., ZHOU J., WANG Y., HU B., LIU Y., KONG L.B., ZHANG T. Embedded MoS_2-PANI nanocomposites with advanced microwave absorption performance. Composites Science and Technology, **198**, 108239, **2020**.
15. LI Z., YU D., WANG X., LIU X., XU Z., WANG Y. A novel strategy of tannery sludge disposal-converting into biochar and reusing for Cr (VI) removal from tannery wastewater. Journal of Environmental Sciences, **138**, 637, **2024**.
16. BENAOUNE S., MERZOUGUI A., REMMANI R., BOUZIDI N., RUIZ-CANALES A., AKACHA I., DJELLOULI A. Dual-Activated Tamarix Gallica-Derived Carbons for Enhanced Glyphosate Adsorption: A Comparative Study of Phosphoric and Sulfuric Acid Activation. Materials, **18**, 511, **2025**.
17. ELEBO A., EKWUMEMGBO P.A., ELAOYI D.P., JIBUNOR V.U., AREGUAMEN O.I. Isotherm and Kinetic investigations of toxic metal decontamination from biofluid by untreated biosorbent using a Batch design. Journal of Chemistry Letters, **4** (2), 71, **2023**.
18. ZHANG H., ZHONG W., QIU R., HAN L. Kinetics and modeling of Pb (II) adsorption in pellet biochar based on micro-computed tomography characterization. Bioresource Technology, **387**, 129645, **2023**.
19. XU C., XU Y., ZHONG D., CHANG H., MOU J., WANG H., SHEN H. Zr^{4+} and glutaraldehyde cross-linked polyethyleneimine functionalized chitosan composite: Synthesis, characterization, Cr (VI) adsorption performance, mechanism and regeneration. International Journal of Biological Macromolecules, **239**, 124266, **2023**.
20. SINGH S., NAIK T.S.S.K., THAMARAISELVAN C., BEHERA S.K., PAVITHRA N., NATH B., DWIVEDI P., SINGH J., RAMAMURTHY P.C. Applicability of new sustainable and efficient green metal-based nanoparticles for removal of Cr (VI): Adsorption anti-microbial, and DFT studies. Environmental Pollution, **320**, 121105, **2023**.
21. GIRISH C.R. Determination of thermodynamic parameters in adsorption studies: a review. Chemical Papers, **79** (9), 5687, **2025**.
22. GUO W., LI P., ZHANG Y., ZHANG Z., WANG W., FAN G., CAO Y., TENG D. One-step room-temperature synthesis of amorphous TiO_2-based adsorbent for enhanced Ge (IV) recovery. Journal of Environmental Chemical Engineering, **13** (1), 115344, **2025**.
23. ZHAO B., GAO B., SHI H., XUE Y., CHEN N., XU H., XING Y.L., ZHAO X., MA B., LIU J., LI J. In situ removal of Cr^{6+} with an intelligent adsorbent: Microwave synthesis, interface adsorption, thermodynamics, mechanism and self-regeneration. Journal of Environmental Chemical Engineering, **12** (2), 112045, **2024**.
24. MASUKU M., NURE J.F., ATAGANA H.I., HLONGWA N., NKAMBULE T.T.I. Pinecone biochar for the Adsorption of chromium (VI) from wastewater: Kinetics, thermodynamics, and adsorbent regeneration. Environmental Research, **258**, 119423, **2024**.
25. LIU Y., SHAN H., PANG Y., ZHAN H., ZENG C. Iron modified chitosan/coconut shell activated carbon composite beads for Cr(Ⅵ) removal from aqueous solution. International Journal of Biological Macromolecules, **224**, 156, **2023**.
26. WANI A.A., KHAN A.M., MANEA Y.K., SALEM M.A., SHAHADAT M. Selective adsorption and ultrafast fluorescent detection of Cr (VI) in wastewater using neodymium doped polyaniline supported layered double hydroxide nanocomposite. Journal of Hazardous Materials, **416**, 125754, **2021**.

27. UMEJURU E.C., PRABAKARAN E., PILLAY K. Coal fly ash decorated with graphene and polyaniline nanocomposites for effective adsorption of hexavalent chromium and its reuse for photocatalysis. ACS Omega, **8** (20), 17523, **2023**.
28. ZHOU H., MA M., ZHAO Y., BAIG S.A., HU S., YE M., WANG J. Integrated green complexing agent and biochar modified nano zero-valent iron for hexavalent chromium removal: A characterisation and performance study. Science of the Total Environment, **834**, 155080, **2022**.
29. WANG X., TAN Z., SHI S., ZHANG S., YANG S., ZHANG X., GAO P., ZHANG, Y. Preparation of Cellulose-Grafted Acrylic Acid Stabilized Jujube Branch Biochar-Supported Nano Zero-Valent Iron Composite for Cr (VI) Removal from Water. Nanomaterials, **15** (6), 441, **2025**.
30. PAZOKI H., ANBIA M. Kinetic and isotherm studies of cr (VI) adsorption from aqueous media by using a synthetic chitosan-allophane nanocomposite. Scientific Reports, **15** (1), 11088, **2025**.
31. KHUSHK S., ZHANG L., LI A., IRFAN M., ZHANG X. Microwave-assisted hydrothermal carbonization of furfural residue for adsorption of Cr (VI): Adsorption and kinetic study. Polish Journal of Environmental Studies, **29** (2), 1671, **2020**.
32. RAMYA V., MURUGAN D., LAJAPATHIRAI C., MEENATCHISUNDARAM S., ARUMUGAM S. A composite adsorbent of superparamagnetic nanoparticles with sludge biomass derived activated carbon for the removal of chromium (VI). Journal of Cleaner Production, **366**, 132853, **2022**.
33. SANGKARAK S., KITTIPONGVISES S., KITKAEW D., CHAVEANGHONG S., ITTISUPORNRAT S., PHETRAK A., LOHWACHARIN J. Influence of the iron-oxide mass fractions of magnetic powdered activated carbon on its hexavalent chromium adsorption performance in water. Chemosphere, **364**, 142997, **2024**.
34. SAMAL P.P., DAS S., QAIYUM M.A., GHOSH A., DEY B., DEY S. Polypyrrole-embedded magnetic Neolamarckia cadamba flower biochar for outstanding Cr (VI) removal from wastewater. Biomass Conversion and Biorefinery, **15** (3), 3429, **2025**.
35. LIU X.Q., ZHANG Y.Y., LIU Y., ZHANG T.A. Green method to synthesize magnetic zeolite/chitosan composites and adsorption of hexavalent chromium from aqueous solutions. International Journal of Biological Macromolecules, **194**, 746, **2022**.
36. YANG X., MU Y., ZHANG L., SUN D., JIAN T., TIAN W. Polyethyleneimine Modified Expanded Vermiculite-Supported Nano Zero-Valent Iron for Cr (VI) Removal from Aqueous Solution. Materials, **18** (13), 2930, **2025**.
37. LIU X., LIU H.L., CUI K.P., DAI Z.L., WANG B., WEERASOORIYA R., CHEN X. Adsorption-Reduction of Cr(VI) with Magnetic Fe-C-N Composites. Water, **15** (12), 2290, **2023**.
38. JUTURU R., VINAYAGAM R., MURUGESAN G., SELVARAJ R. Synthesis and characterization of Zn and Fe doped magnetic biochar from Acacia falcata leaves for Cr (VI) adsorption. Scientific Reports, **15** (1), 22146, **2025**.
39. SUN H., WANG L., WANG X., DONG Y., XIN J., REN J., AN J., JING R. Construction of recyclable magnetic PEI-modified GO/Fe_3O_4 adsorbents for high-efficient removal of Cr (VI) ions from aqueous solutions. Solid State Sciences, **154**, 107611, **2024**.
40. SAEED Z.T., MAJED Z.W., ALTAMER D.H., FADHIL A.B. Preparation of nano-magnetic activated biochar from Vicia faba Peel: application for Eriochrome Black T and Cr (Ⅵ) removal from aqueous phases. International Journal of Environmental Analytical Chemistry, **105** (18), 7285, **2025**.
41. PAN J., SUN H., CHEN K., ZHANG Y., SHAN P., SHI W., GUO F. Nanodiamonds decorated yolk-shell $ZnFe_2O_4$ sphere as magnetically separable and recyclable composite for boosting antibiotic degradation performance. Chinese Journal of Chemical Engineering, **54**, 162, **2023**.
42. GAO J., LIU X., REN P., GAO J., CHEN Y., CHEN Z. Removal behavior and mechanism of amino/carboxylate-functionalized Fe@SiO_2 for Cr(Ⅵ) and Cd(II) from aqueous solutions. Environmental Science and Pollution Research, **29** (47), 72058, **2022**.
43. SONKAWADE R.G., WAIKAR M.R., SHAIKH A.A., SHIRSAT M.D., ALI Y., CHAKARVARTI S. K. Effect of low energy li-negative ions irradiation on electrochemically synthesized copper nanoflakes/polyaniline nanofibers composite thin film. Thin Solid Films, **730**, 138710, **2021**.
44. FAN S., ZHANG Y., JI P., HU X., ZHAO M., ZHOU N. Revealing the pivotal role of surface functional groups in Cr (VI) photocatalytic removal by pristine sludge biochar under visible light. Research on Chemical Intermediates, **52**, 2195, **2026**.
45. BABAKHANI A., PEIGHAMBARDOUST S.J., GHAHREMANNI-NASAB M., PEIGHAMBARDOUST N.S. Fabrication of biodegradable nanocomposite scaffolds with hydroxyapatite, magnetic clay, and graphene oxide for bone tissue engineering. Scientific Reports, **15** (1), 22235, **2025**.
46. ZHANG X., ZHANG Q., SU H., XU Y., LI L. Nanoparticle-decorated and poly (dimethyl siloxane)-modified superhydrophobic melamine sponge for efficient oil/water separation. Materials Chemistry and Physics, **304**, 127909, **2023**.
47. ATINAFU D.G., YUN B.Y., KIM Y.U., WI S., KIM S. Introduction of eicosane into biochar derived from softwood and wheat straw: Influence of porous structure and surface chemistry. Chemical Engineering Journal, **415**, 128887, **2021**.
48. TASHEVA T., HARIZANOVA R., MIHAILOVA I., CHERKEZOVA-ZHELEVA Z., PANEVA D., NEDKOVA M., RÜSSEL, C. Structure and redox ratio of soda‐lime‐silica glasses with high iron oxide concentrations. International Journal of Applied Glass Science, **14** (3), 445, **2023**.
49. BETTAYEB B., BELAMRI D., BENHAMIDA S., BENKRIMA Y., BENMENINED A., MANSERI A. Effect Of Temperature Deposition On The Properties Of Zno Thin Films Prepared By Low-Cost Nebulizer Spray Pyrolysis Method. Nanotechnology Perceptions, **20** (6), 183, **2024**.
50. ZHENG C.L., WANG Q.R., GENG G.Q., WANG Z.X., ZHUO H. Adsorption of lead ions by a kind of MAL modified hydrogel beads. Transactions of Nonferrous Metals Society of China, **32** (8), 2770, **2022**.
51. LEE S.P., ALI G.A.M, ASSIRI M.A., KONG K.V., TEO E.Y.L., CHONG K.F. Pseudocapacitive performance of phenothiazine functionalized graphene aerogel. Applied Surface Science, **613**, 156069, **2023**.
52. KUTE A.D., KALE H.B., GAWANDE M.B. Iron N‐Doped Carbon Nanoarchitectonics for C-H Bond Activation of Methylarenes and Esterification Reactions. Small, **21** (16), e2409707, **2025**.
53. SHEN H., ZHONG D., XU Y., CHANG H., WANG H., XU C., MOU J., ZHONG N. Polyacrylate stabilized ZVI/Cu

bimetallic nanoparticles for removal of hexavalent chromium from wastewater. Environmental Science and Pollution Research, **30** (3), 5847, **2023**.
54. ZHANG J., ZHANG T., SONG W., YU R., SHEN W. MEMS-based Au-PANI gas sensor with enhanced NH_3 sensitivity and humidity tolerance at room temperature. Materials Letters, **405**, 139777, **2026**.
55. OZALP O., GUMUS Z.P., SOYLAK M. Metal‐organic framework functionalized with deep eutectic solvent for solid‐phase extraction of Rhodamine 6G in water and cosmetic products. Journal of Separation Science, **46** (19), e2300190, **2023**.
56. ZHANG Z., ZHOU Q., ZHOU L., LIU Y., WANG Z., BAO S., WANG L., HUA X., WEI R. Hot‐Stretching of Barium Titanate and Poly (Arylene Ether Nitrile) Composites for Enhanced Energy Storage Density. Polymer Composites, **47** (8), 6979, **2026**.
57. HUERTA F., QUIJADA C., MONTILLA F., MORALLÓN E. Revisiting the redox transitions of Polyaniline. Semiquantitative interpretation of electrochemically induced IR bands. Journal of Electroanalytical Chemistry, **897**, 115593, **2021**.
58. NANDA D., MOHANTY C., MISHRA P.P., TRIPATHY B.C., DAS N., BEHERA A.K. Synergistic Polyaniline‐Biochar Hybrid Adsorbent for Efficient Detoxification of Organic Dyes and Hexavalent Chromium From Aqueous Solutions. ChemistrySelect, **11** (3), e05010, **2026**.
59. LI G., WANG C., XIE K., WEI X., NIU H. Transformation of Cr (Ⅲ) in different redox environments. Bulletin of Geological Science and Technology, **44** (2), 389, **2024**.
60. KULANDAIVEL S., LU Y.K., LIN C.H., YEH Y.C. Dual-functional PCN-242 (Fe_2Co) MOF for sensitive bacterial endotoxin detection. Journal of Materials Chemistry B, **13** (1), 151, **2025**.
61. YANG S., YE Z., CHENG X., WANG Y., LUAN Z., LI W., HU B. Electro-adsorption and reduction of Uranium (VI) by Fe_3O_4@COFs electrode with enhanced removal performance. Chemical Engineering Journal, **474**, 145598, **2023**.